MATERIALS SCIENCE

A sensitive and robust thin-film x-ray detector using 2D layered perovskite diodes

Hsinhan Tsai[1], Fangze Liu[1], Shreetu Shrestha[1], Kasun Fernando[1], Sergei Tretiak[2,3], Brian Scott[1], Duc Ta Vo[4], Joseph Strzalka[5], Wanyi Nie[1,2]*

Solid-state radiation detectors, using crystalline semiconductors to convert radiation photons to electrical charges, outperform other technologies with high detectivity and sensitivity. Here, we demonstrate a thin-film x-ray detector comprised with highly crystalline two-dimensional Ruddlesden-Popper phase layered perovskites fabricated in a fully depleted *p-i-n* architecture. It shows high diode resistivity of 10^{12} ohm·cm in reverse-bias regime leading to a high x-ray detecting sensitivity up to 0.276 C Gy_{air}^{-1} cm^{-3}. Such high signal is collected by the built-in potential underpinning operation of primary photocurrent device with robust operation. The detectors generate substantial x-ray photon–induced open-circuit voltages that offer an alternative detecting mechanism. Our findings suggest a new generation of x-ray detectors based on low-cost layered perovskite thin films for future x-ray imaging technologies.

INTRODUCTION

Solid-state radiation detectors directly convert x-ray signal into electrical current with superior sensitivity and high count rate that outperform other detection technologies and are critically needed in medical (*1–4*) and security applications (*5–7*) as well as in Advanced Photon Source facilities (*8–10*). In a high-performance x-ray detector, one of the critical requirements is to minimize the dark current amplitude at reverse bias so that current generated at low x-ray dosage can be well resolved above the dark noise, which determines the device detectivity (i.e., the lowest detectable dosage). This will require (i) high-purity semiconductors to suppress thermally activated recombination in the dark via trap states and (ii) fully depleted junctions across active regions to avoid space charge accumulation and interfacial charge recombination. Furthermore, the semiconducting materials used for detector need to be robust, without current drifting or current-voltage hysteresis. Currently, this is attained using high-purity semiconducting single crystals (*11*) operating under high voltages across active regions (*12*) to efficiently collect generated charges and avoid recombination losses. However, such a detector needs a high operational voltage across a large thickness (~1 cm), which has issues like charge drifting under or high fabrication cost for obtaining large volumes of monocrystals that undermine their use in scalable imaging application.

RESULTS AND DISCUSSION

Here, we design a new type of thin-film device made in *p-i-n* junction configuration with two-dimensional (2D) Ruddlesden-Popper (RP) phase layered perovskite $(BA)_2(MA)_2Pb_3I_{10}$ (Pb3) (Fig. 1A) to efficiently detect x-ray photons. As illustrated in Fig. 1A, the device uses a structure of indium tin oxide (ITO)/p-type contact/2D RP thin film/n-type contact/gold, where we chose poly[bis(4-phenyl)(2,4,6-trimethylphenyl)amine] (PTAA) as p-type contact and C_{60} as n-type contact. The synchrotron grazing incidence wide-angle x-ray scatter-ing (GIWAXS) measurement shown in Fig. 1B further confirms the superior crystalline and preferred orientation in the 2D RP thin film (*13*, *14*). To evaluate the feasibility of perovskites as a radiation detector, we calculate linear x-ray absorption coefficient (μ_l) as a function of incident energy (details can be found in Materials and Methods) for our 2D RPs, 3D methylammonium lead tri-iodide perovskite ($MAPbI_3$), and silicon (Si) and plot them in Fig. 1C. The absorption coefficient of these perovskite materials is, on average, 10- to 40-fold higher than that of silicon for hard x-ray. Note that the μ_l for both 2D and 3D perovskites are similar; this suggests that the presence of the large organics in the 2D perovskites does not affect the x-ray absorption coefficients, which are dominated by the heavy elements. Taking advantage of such strong x-ray absorption at perovskite materials (fig. S1), we then test the thin-film *p-i-n* detector under x-ray. The 2D RP x-ray absorber layers are fabricated with hot casting approach (*14–16*) that formed a highly crystalline thin film to achieve enhanced charge transport and collection across the two electrodes (*17*).

Figure 1 (D to F) summarizes the detector's performance made with the 470-nm 2D RP thin film when measuring in the dark and under synchrotron beam with a mono energy of 10.91 keV and a photon flux of 2.7×10^{12} photon counts per square centimeter per second (Ct cm^{-2} s^{-1}) (x-ray photon flux calibration is described in Materials and Methods). As a reference, we have also measured the commercial silicon *p-i-n* diode (600 μm thick) under the same condition. The current density–voltage characteristics (*J-V*) in the dark and under x-ray exposure as plotted in Fig. 1D are used to describe the devices' responses. Benefitting from the *p-i-n* junction design, the dark current density for the 2D RP device is as low as 10^{-9} A cm^{-2} at zero bias and 10^{-7} A cm^{-2} at −1 V, which translates to a high dark resistivity of 10^{12} ohm·cm coming from the diode because of the efficient dark current blocking layers. Note that the material's intrinsic dark resistivity is calculated to be 5×10^{12} ohm·cm by the forward-injection regime (fig. S2). Once the devices are exposed to the x-ray source, the 2D RP device shows a giant increase in x-ray–induced current density (J_X) at zero bias (short circuit), four orders of magnitude higher than dark current (Fig. 1D). As a comparison, we placed the Si device under the same x-ray exposure condition that only outputs an increase of two orders of magnitude in J_X (Fig. 1D, black). Notably, the Pb3 devices are hysteresis free in the dark and under x-ray illumination (fig. S3). The 2D RP device also generates a large open-circuit voltage (V_{OC}) of ~650 mV under x-ray exposure, while that for the Si diode

[1]Materials Physics and Applications Division, Los Alamos National Laboratory, Los Alamos, NM 87544, USA. [2]Center for Integrated Nanotechnologies, Los Alamos National Laboratory, Los Alamos, NM 87545, USA. [3]Theoretical Division, Los Alamos National Laboratory, Los Alamos, NM 87544, USA. [4]Nuclear Engineering and Nonproliferation, Los Alamos National Laboratory, Los Alamos, NM 87544, USA. [5]X-Ray Science Division, Argonne National Laboratory, Argonne, IL 60439, USA.
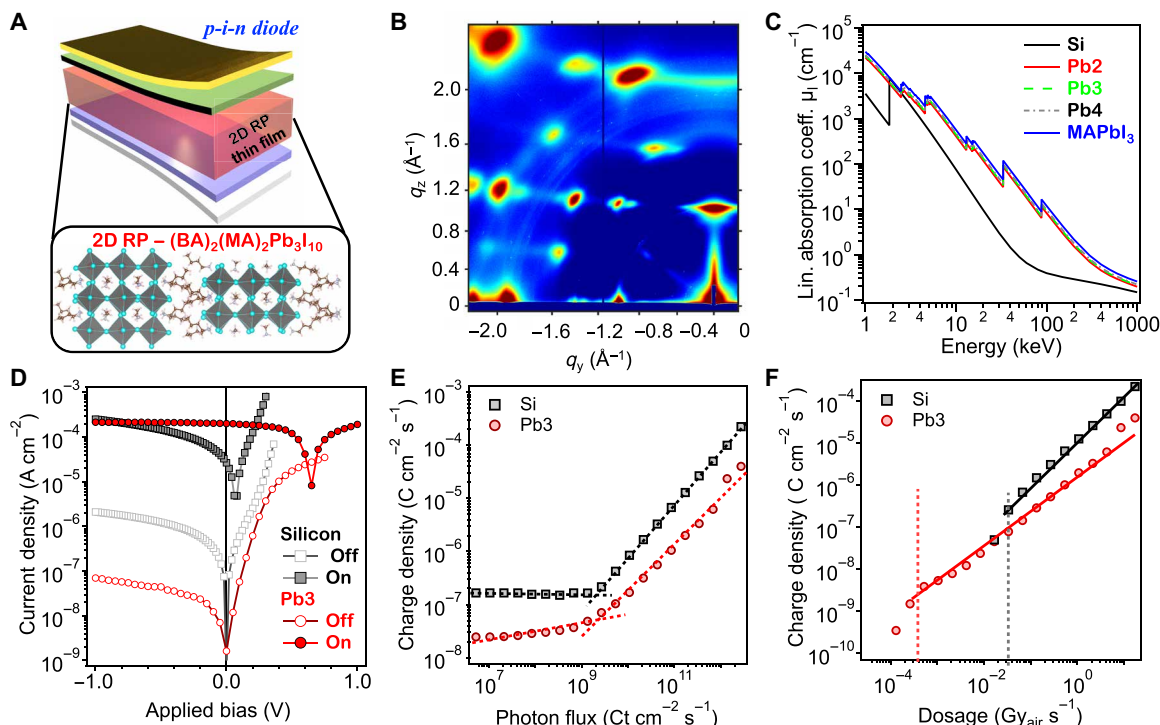*Corresponding author. Email: wanyi@lanl.gov

Fig. 1. Thin-film x-ray detectors and their properties. (**A**) Schematic illustration of the 2D RP–based *p-i-n* thin-film x-ray detector device architecture composed of $(BA)_2(MA)_2Pb_3I_{10}$ (dubbed as Pb3) as an absorbing layer. (**B**) GIWAXS map of the 2D RP thin film done under synchrotron beam. (**C**) Calculated linear x-ray absorption coefficient (μ_l) as a function of incident radiation energy for hybrid perovskite materials and silicon. (**D**) *J-V* characteristic for 2D RP and silicon reference devices in the dark and under x-ray (10.91 keV) exposure. (**E**) X-ray–generated charge density as a function of x-ray dosage for 2D RP (red) and silicon diode (black) under zero bias. (**F**) X-ray–induced charge density subtracted by the dark noise (signal-to-noise ratio) for 2D RP and silicon reference detector from (E).

was merely ~250 mV. Both the high V_{OC} and large J_X produced at short circuit are attributed to the high density of charge carriers generated in 2D RP accredited to the high-absorption cross section and low nonradiative recombination in the crystalline thin film.

To quantify the detector's detection limit, we further extracted the charge density from J_X under zero bias with various x-ray photon fluxes for 2D RP and a silicon device, and they are plotted in Fig. 1E. The detecting photon density limit for the 2D RP device is about 5×10^8 Ct s^{-1} cm^{-2}. Compared with a Si reference device (3×10^9 Ct s^{-1} cm^{-2}), this value is lower owing to the low dark current for the former. We further calculate the ionization energy (W) for 2D RP material to validate the results based on the following relation

$$W = \frac{\varphi \times E \times \eta}{Q/q}$$

where φ is the photon flux (Ct s^{-1} cm^{-2}), E is the x-ray photon energy (eV), η is the material's absorption efficiency, Q is the total charge density extracted (C cm^{-2} s^{-1}), and q refers to elementary charge. By fitting Fig. 1E linearly, we obtained the estimated value for W to be 4.46 eV (see Materials and Methods for the detailed calculations). Several materials follow the Klein rule (*18*), which gives an estimate of the relationship between the ionization energy and bandgap of the material as: $W_{\pm} = 2.8 * E_g + E_{phonon}$, where E_g is the energy bandgap (1.8 eV for Pb3) and E_{phonon} is the phonon energy term (approximately 0.5 eV). Using the Klein rule, the value of $W_{\pm}$ for Pb3 is 5.54 eV. Our measured value (4.46 eV) is in the same range as the theoretically predicted value.

An important figure of merit is the detector's sensitivity (C Gy_{air}^{-1} cm^{-3}), which can be extracted from the slope of a linear region in the charge density–dosage–dependent plot in Fig. 1F and multiplied by the active layer thickness. We first convert the photon flux into exposure dosage for air (Gy_{air}) by calculating the charge ionized in air with 10.91 keV x-ray energy (see Materials and Methods). Then, the x-ray signal subtracted by the dark signal from the detector ($C_{on} - C_{off}$) is plotted in Fig. 1F as a function of incident x-ray dosages. We observe that the 2D RP device has a comparable signal-to-noise level at high x-ray dosage to Si diode, whereas it shows a much lower detecting limit with a distinguishable signal-to-noise ratio of 10^{-8} charge density (C cm^{-2} s^{-1}) at low exposure dosage down to 10^{-5} Gy_{air} s^{-1}. By multiplying the slope and the active layer thickness, the sensitivity for the 2D RP device is estimated to be 0.276 C Gy_{air}^{-1} cm^{-3}. The sensitivity value for the Si *p-i-n* diode in our measurement is comparable to a typical silicon diode performance as thoroughly discussed in Note S3, which validates our measured values here. The sensitivity value for the 2D RP device is considerably higher than other reported sensitivity values for the perovskite thin-film x-ray detectors (see table S1, which presents a detailed comparison with literature-reported detectors) (*19–24*). Also, note that the thin-film detectors offer better performance than the bulk crystal detectors operating in the low x-ray energy regime (*24*), which thus motivates the development of the thin-film detector for those applications. The 2D RP device studied here showing high sensitivity under zero bias is also called primary detecting current and can thus be considered as a self-powered detector.

To understand such superior detector performance, we examine the power- and field-dependent *J-V* characteristics for the 2D RP device in greater detail in Fig. 2 (A and B). The *J-V* curves under various x-ray photon fluxes are plotted in Fig. 2A. As expected, the Pb3 device signals systematically decrease with diminishing photon flux. Under high x-ray exposure, the *J-V* slope flattens in the moderate forward- to reverse-bias regime (see fig. S5 for the derived *J-V* slopes), indicating a field-independent charge collection (*17*). We further plot the J_X as a function of x-ray photon flux under various electrical fields in Fig. 2B. The x-ray photon flux–dependent J_X is found to be nearly identical when the detector operates under different applied voltages (Fig. 2B). Both observations suggest a near-ideal charge collection efficiency under x-ray exposure. Because of the large density of carriers generated by the strong x-ray absorption in Pb3, a large built-in field is formed by quasi-fermi level splitting between *p* and *n* contacts, facilitating the subsequent charge collection. This is thus an intentional benefit of the thin-film *p-i-n* junction design, where charges are collected by an internal electrical field without the need of external fields. The field-independent charge collection holds at various x-ray irradiations (Fig. 2B), which leads to the observation of near-identical J_X–x-ray flux curves under various fields. The results mean that the Pb3 thin-film detector remains efficient at low dosage exposure. To validate our hypothesis, we use capacitance-voltage (*C-V*) measurement to probe the depletion junction for 2D RP thin-film (470 nm) x-ray devices. Figure 2C shows the normalized *C* (the capacitance by C_0 value at 0 bias) against a DC bias curve probed at an AC frequency of 100 kHz. From the plot, we observe a flattened slope in the −1 to +0.9 V range, indicating a negligible change in capacitance under external DC bias in this range. This is a classical signature of a fully depleted junction formation without the contribution of space charge in the intrinsic perovskite layer (*25*). At forward bias, the capacitance value increases after the bias is higher than the flat band voltage. This is due to the charge recombination in the junction by DC current injection.

The fact that our detector produces high open-circuit voltage (V_{OC} = 650 mV) due to high carrier density generation is suggestive of using the generated voltage as an alternative detection parameter. To evaluate the feasibility, we plot V_{OC} values for 2D RP and Si reference detectors as a function of x-ray photon flux under two different energies (Fig. 2, D and E). The range of the x-ray photon flux is estimated by the output current signal from the calibration silicon diode exposed under those two x-ray photon sources. In both plots, the V_{OC} is found to scale linearly with the photon flux in log scale. The open-circuit voltage generation in a photovoltaic device (*26*) was attributed to the quasi-fermi level splitting determined by the balance between carrier generated and recombination, and the value was found to be linearly promotional to the photon flux in log scale. It can be described by the effective bandgap (E_{eff}) and charge recombination (*n*) and is a function of temperature (*T*) (*27*)

$$V_{OC} = \frac{k_B T}{q} \ln\left(\frac{(N_A + \Delta n)\Delta n}{n_i^2}\right)$$

where $k_B T/q$ is the thermal voltage, N_A is the doping concentration, Δn is the excess carrier concentration, and n_i is the intrinsic carrier concentration. During photovoltaic device operation, the photo-generated carrier concentration is proportional to the incident light power,
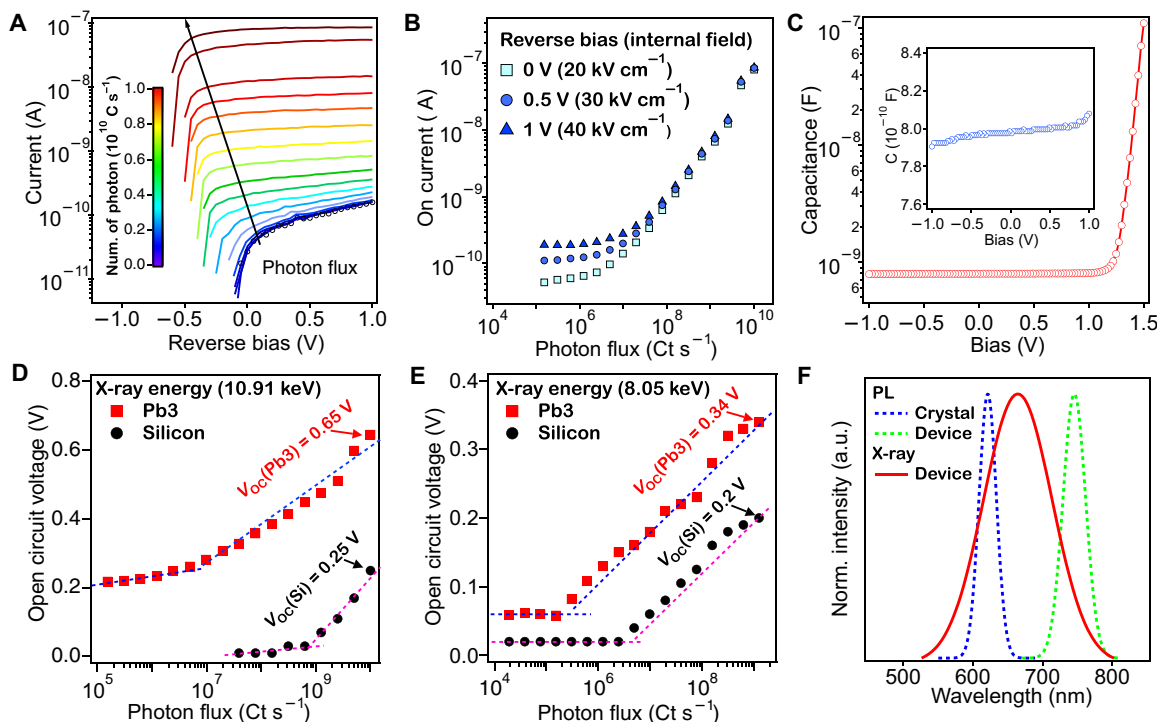

Fig. 2. Device characteristics. (**A**) Power-dependent *J-V* characteristics for 2D RP thin-film x-ray detector response with Pb3 as an absorbing layer (470-nm thickness) under various photon fluxes. (**B**) On-current at various reverse biases as a function of photon flux in unit of counts per second (Ct s^{-1}) for the 2D RP device. (**C**) Capacitance-voltage curve for the 2D RP thin-film device (470 nm). The capacitance is normalized by its capacitance at 0 bias. Open-circuit voltage (V_{OC}) as a function of normalized x-ray beam flux in log scale for different energy values of (**D**) 10.91 keV and (**E**) 8.05 keV for 2D RP (470 nm) and silicon reference devices. (**F**) Photo emission spectra of the Pb3 thin-film device excited by hard x-ray (red) as compared to the photoluminescence spectra of the Pb3 thin film (green) and the Pb3 single crystal (blue) excited by laser (405 nm). a.u., arbitrary units.

and the open-circuit voltage is thus proportional to the ln (power). A similar trend was observed in Fig. 2 (D and E), where the V_{OC} scales linearly with the log of the incident x-ray photon flux. Therefore, the x-ray–generated open-circuit voltage is also a charge density–dependent term. By fitting the linear-log curve in Fig. 2D, the obtained slope is 0.046, corresponding to $2 k_B T/q$ at room temperature; here, k_B is Boltzmann constant, T is temperature, and q refers to elementary charge. This is a similar observation to our previous study (17) in that, at lower light power, the 2D perovskite device's V_{OC} versus log-light power plot yields a linear fit slope of $2 k_B T/q$ at room temperature. Such relation is concomitant to our observation in x-ray detectors, suggesting that the physical origin of the x-ray–generated V_{OC} is determined by the charge density as well.

We further measured the x-ray luminescence spectra of the Pb3 thin film (Fig. 2F, red) by probing the visible emission signal from the Pb3 thin film under x-ray excitation. This measurement reveals the ionized charge recombination pathway (radiative recombination) that helps to gain deeper insight into the detector operational mechanism. The intrinsic emission spectra for Pb3 single crystal and thin films by photoluminescence (PL) are compared in the same plot. It is interesting to observe that the Pb3 thin film exhibits a broad spectrum upon x-ray excitation, covering energies from 2 to 1.66 eV. Note that the thin film is stable after this measurement is checked by the crystalline structure with a GIWAXS map (fig. S6) that excludes the degradation effect. From the literature, it is known that the 2D RP thin film has two PL emission features at both high-energy (peaks at 2 eV) and low-energy states (peaks at 1.7 eV). The high-energy feature is observed from the single crystal (bulk states), whereas the low-energy emission state dominates in the thin film, and the latter facilitates the carrier dissociation and prevents charge recombination (28). When comparing the x-ray luminescence spectra of the Pb3 thin film to the PL of the film (green) and single-crystal flakes (blue), the emission originates from ionized charge recombination from both low-energy and high-energy states. This was not observed in the PL spectra when excited by low-energy lasers. We therefore conclude that, when high-energy x-ray excites the material, the charges are avalanched and ionized at a much higher energy (high density of hot carriers) and transport through both high-energy and low-energy states to be collected directly that yields electrical signal. This is distinctive to the detector operating under visible light where hot-carrier loss is not avoidable. Such process thus benefits a high x-ray–induced electrical-current signal and high V_{OC} generation without thermal loss through a hot-carrier cooling process in the Pb3 device, which demonstrates an outstanding performance in an x-ray detection mode as opposed to visible-light detection (figs. S7 to S9).

To summarize here, the linear dependence observed in Fig. 2 (D and E) suggests V_{OC} as a promising detecting mechanism that can advance a much-simplified external circuit design for signal measurements. Notably, our 2D RP device shows distinguishable V_{OC} at different x-ray energies, which could thus be a sensitive parameter to distinguish the energy through different numbers of ionized carriers in the semiconductor (29, 30).

One of the expectations using solid-state x-ray detector is their fast response time to x-ray exposure. However, the reported state-of-the-art x-ray detector based on perovskite materials has a response time in the second to millisecond regime because of the presence of hysteresis effect (19–24). In the 2D RP device, the thin-film design with a large built-in field should facilitate the fast extraction of x-ray–generated carriers, presenting another advantage of such device design. We therefore used visible light as an excitation source to test the detector's
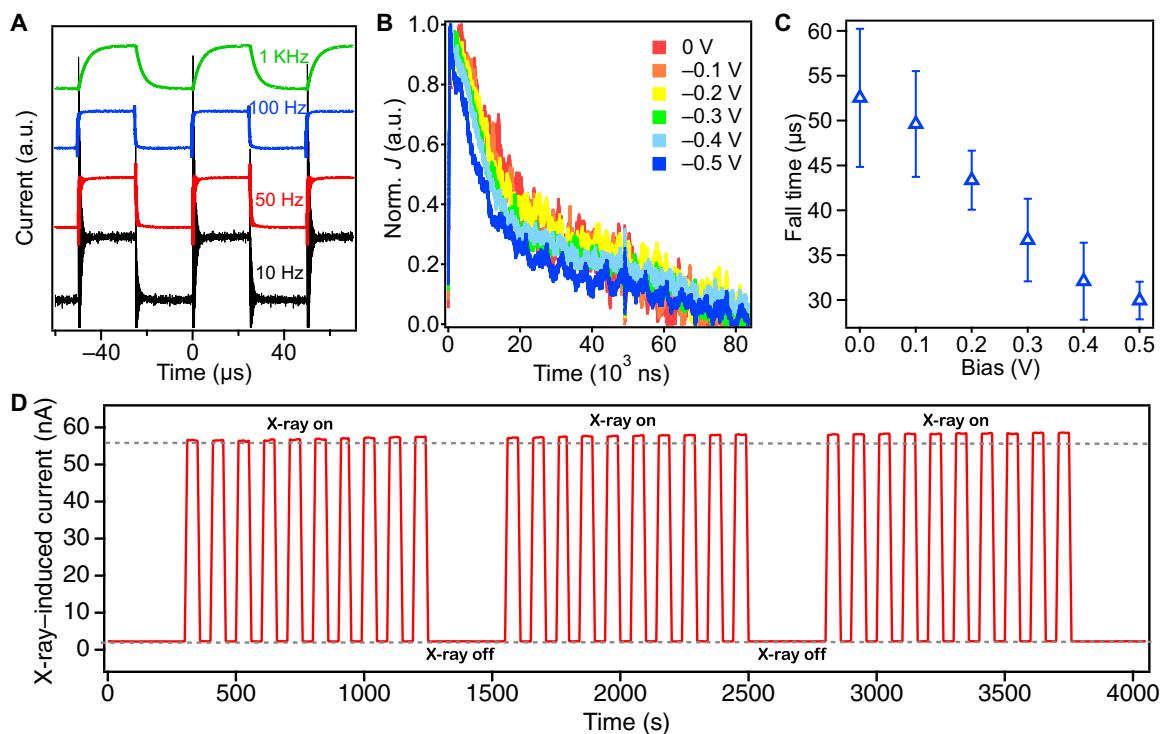

Fig. 3. Devices' temporal responses and stabilities. (**A**) Transient photocurrent response of device with various applied resistance. (**B**) Time-resolved photo conductivity of a thin-film device under pulsed-laser excitation (375 nm). (**C**) Device signal fall time extracted from (**B**) under various biases. (**D**) Stability test of the thin-film detector operating under continuous hard x-ray (10.91 keV) exposure under short circuit conditions.

temporal response with various load resistors (Fig. 3A). The rise and fall times are found in the range of 1 to 10 μs and become slower as the load resistor increases. This indicates that the detectors' temporal response is capped by the circuit time constant and that the real response from the material is much faster. We therefore further investigated the time-resolved photocurrent under fast laser excitation, and the photocurrent amplitude was kept comparable to the x-ray–induced current density (0.1 mA cm^{-2}). The rise time of the device under pulsed laser is <500 ns and fall time is in the range of 20 to 60 μs (Fig. 3, B and C), and external applied bias speeds up the detector response as expected. This is much faster than the literature-reported detector using bulk film or crystal as an absorber and can be attributed to the *p-i-n* junction design. It is also related to the greatly reduced defect in the highly crystalline 2D RP perovskite thin film that suppresses the ion migration–induced current hysteresis (fig. S3).

The primary photocurrent feature of our thin-film detector allows the device to efficiently operate without bias. It is well known that perovskites are unstable under high voltage. However, high-voltage operation is required in a bulk detector with a large volume, which drastically reduces the device operational lifetime. In our case, the thin-film device performance is stabilized for 30 cycles of voltage scans and x-ray exposures (Fig. 3D). We scanned the dark and x-ray current-voltage characteristics 30 times, with each dark and exposure time of 300 s (fig. S6A in SI for *J-V* curves). The dark current remains the same after the 30 scans, suggesting that the junction remains robust after voltage cycling. The device first exhibited an increase in x-ray photo current, while the dark current remained unchanged. We have also examined the crystalline structure by GIWAXS on the thin film before and after the stability tests. In addition, the GIWAXS patterns remain identical (fig. S6, B and C), which suggests that the thin film is stable under both bias and x-ray exposure.

As a summary, we demonstrate that a high-quality layered perovskite thin film makes a promising candidate for radiation detector. The thin-film device design allows for low dark current to enable high sensitivity with improved detection limit. The device operates with low external bias leading to a stable detection performance, which can be valuable for low-energy x-ray and ion detections for space science. Last, we notice that for higher-energy x-ray detection, a much thicker layer is needed. We have attempted to fabricate a film with a thickness of 8 μm; the thick film maintains the crystallinity (see figs. S10 and S11), and other coating protocols could fabricate thicker 2D perovskite films with high quality, making them useful for high-energy x-ray detection applications (*31*).

MATERIALS AND METHODS
Materials and instruments
Lead oxide (PbO), methylamine hydrochloride (MACl), hydriodic acid (HI, 57 weight % in H_2O), hypophosphorous acid (H_3PO_2, 50% in H_2O), butylamine (BA, 99%), C_{60}-Fullerene, PTAA, and *N,N*-dimethylformamide (DMF, anhydrous) were purchased from Sigma-Aldrich and used without further purification. Tektronix Keithley 2400 SMU was used for data collection. The silicon reference device (FDS 1010 Si Photodiode) was purchased from Thorlabs.

2D RP material preparation
Raw 2D layered perovskite materials were prepared by combining PbO, MACl, and BA in appropriate ratios in a HI/H_3PO_2 solvent mixture as described in previous reports (*32–34*). The materials were characterized with an x-ray diffraction for purity and desired *n*.

Detector fabrication
Pb3 solutions were prepared with molar concentrations of 2, 1, 0.5, and 0.25 M Pb^{2+} cations in anhydrous DMF. ITO glasses were cleaned using an ultrasonication bath in soap water; rinsed progressively with distilled water, acetone, and isopropyl alcohol; and lastly treated with oxygen plasma for 5 min and then transferred to an argon-filled glove box (*35, 36*). The PTAA layer was then spin-coated onto the precleaned ITO substrates at 2000 rpm for 45 s as a hole-transporting layer. The 2D perovskite solutions were prepared by dissolving a 2D perovskite single crystal in anhydrous DMF. The thin-film fabrication was followed by the hot-casting process (*13–16, 36, 37*). The C_{60} layer and the Au electrode (0.04 cm^2) were deposited using a thermal evaporator.

Linear x-ray absorption coefficient calculation
The absorption coefficient μ of a compound is the sum of the mass fractions of all elements in the compound

$$\mu = \sum_i f_i \mu_i = \frac{\sum_i N_i A_i \mu_i}{\sum_i N_i A_i}$$

where *i* denotes the elements of the compound, f_i is the mass fraction of element *i*, μ_i is the absorption coefficient of element *i*, N_i is the number of atoms of element *i* in the compound, and A_i is the atomic weight of element *i*.

For MAPbI$_3$ (CH$_3$NH$_3$PbI$_3$), its empirical formula can be expressed as CNH$_6$PbI$_3$. Then, the absorption coefficient μ will be

$$\mu_{MAPbI_3} = \frac{(A_C \mu_C + A_N \mu_N + 6A_H \mu_H + A_{Pb} \mu_{Pb} + 3A_I \mu_I)}{(A_C + A_N + 6A_H + A_{Pb} + 3A_I)}$$

The absorption coefficients for the 2D RP devices are determined the same way.

$$\mu_{(BA)_2(MA)_1Pb_2I_7} = \frac{(9A_C \mu_C + 2A_N \mu_N + 30A_H \mu_H + 2A_{Pb} \mu_{Pb} + 7A_I \mu_I)}{(9A_C + 2A_N + 30A_H + 2A_{Pb} + 7A_I)}$$

$$\mu_{(BA)_2(MA)_2Pb_3I_{10}} = \frac{(10A_C \mu_C + 3A_N \mu_N + 36A_H \mu_H + 3A_{Pb} \mu_{Pb} + 10A_I \mu_I)}{(10A_C + 3A_N + 36A_H + 3A_{Pb} + 10A_I)}$$

$$\mu_{(BA)_2(MA)_1Pb_2I_7} = \frac{(11A_C \mu_C + 4A_N \mu_N + 42A_H \mu_H + 4A_{Pb} \mu_{Pb} + 13A_I \mu_I)}{(11A_C + 4A_N + 42A_H + 4A_{Pb} + 13A_I)}$$

The unit for the absorption coefficient μ is cm^2/g. It is sometimes simpler to use the linear absorption coefficient μ_l, which has a unit of 1/cm (Fig. 1B). $\mu_l = \mu * \rho$, where ρ is the density of the material. The mass densities of materials (ρ) used in Fig. 1B are 2.329 g/cm^3 (silicon), 4.130 g/cm^3 (MAPbI$_3$) (*38*), 3.159 g/cm^3 (BA$_2$MAPb$_2$I$_7$), 3.392 g/cm^3 (BA$_2$MA$_2$Pb$_3$I$_{10}$), and 3.543 g/cm^3 (BA$_2$MA$_3$Pb$_4$I$_{13}$) (*33*), respectively.

Detector measurement setup
Synchrotron x-ray has a mono energy of 10.91 keV with a photon flux of 4.6×10^{10} Ct s^{-1}. The various incident photon fluxes are controlled by changing a series of Al foils of varying thicknesses, which allowed the attenuation of the desired beam flux during measurements. The

footprint of the beam is 20 mm by 0.2 mm with a 0.15° incident angle. Parts of experiments were performed with a Bruker D8 advance x-ray diffractometer with an x-ray energy of 8.05 keV with 2θ = 45°.

Ionization energy calculation

$$\text{Ionization energy}\ (W_\pm) = \frac{\text{total energy absorbed}}{\text{total e} - \text{h pairs created}}$$

Here, we have total e-h pairs created (Eq. 1) and total energy absorbed (Eq. 2) (39)

$$\text{Total e} - \text{h pairs created} = \frac{Q}{q} \tag{1}$$

Total energy absorbed =

photon density × photon energy × device quantum efficiency (2)

where the device quantum efficiency η = 1 − exp(− μd), linear attenuation coefficient for the photon energy used (μ) = 473 cm^{-1}, and device thickness (d) = 500 nm. Therefore, by dividing Eq. 1 from Eq. 2, we get

$$W_\pm = \frac{\text{photon density} \times \text{photon energy} \times \text{device quantum efficiency}}{\frac{\text{charge extracted}}{q}}$$

$$= \frac{1}{\text{slope}} \times \text{photon energy} \times \text{device quantum efficiency} \times q$$

$$= 4.46\ \text{eV}$$

where the slope is obtained from the linear fit in Fig. 1E (also see fig. S4 for the linear fit), photon energy is 10910 eV, and charge extracted is 2.73×10^{-8} C cm^{-2} s^{-1}.

X-ray dosage calculation

Synchrotron-based characterization of the devices took place at beamline 8-ID-E of the Advanced Photon Source, Argonne National Laboratory (40). Beamline 8-ID-E is insertion device–based with two APS Undulator A units operated in tandem as the source, which is shared with beamline 8-ID-I. A single-bounce monochromator Si (111) crystal intercepts half of the beam and directs the component with photon energy E = 10.91 keV into the GIWAXS instrument. Samples were investigated in a vacuum sample environment (3×10^{-3} torr) for GIWAXS that is coupled to the beamline with flexible vacuum bellows, so there are no windows between the x-rays and the sample, except for a highly polished Be window separating the beamline vacuum from the vacuum at the monochromator and further upstream. Two sets of in-vacuum slits (JJ X-ray A/S) defined the size of the beam as 200 μm by 20 μm (H by V), with a third set of in-vacuum slits as guard slits. A series of Al foils of varying thicknesses mounted in two sets of pneumatically operated filter banks positioned between the first and second set of slits allowed us to attenuate the beam as desired during measurements. We measured the unattenuated x-ray flux at a position in between the second and third set of slits with a calibrated p-i-n diode to be $(4.61 \pm 0.05) \times 10^{10}$ ph/s with the storage ring current operating at 101.8 mA, in top-up operations mode. This p-i-n diode was retracted during measurements of the sample. During measurements, the x-ray beam impinged on the sample in grazing incidence, with incident angle α$_i$ =

0.15°, resulting in an x-ray footprint on the sample of 200 μm by 8 mm. In this manner, the fluence of the beam was reduced from a maximum of $(1.15 \pm 0.01) \times 10^{13}$ to $(3.02 \pm 0.03) \times 10^{10}$ ph/mm^2. The perovskite-based p-i-n diode devices tested were fabricated to dimensions of 2 mm by 2 mm to capture all of the incident x-ray beam. The commercial p-i-n diodes tested for comparison had dimensions of 100 mm by 2 mm. Samples were tested under vacuum at temperature 25°C as maintained by a Linkam HFSX350-GI stage with liquid nitrogen cooling.

The dosage calculation for monoenergetic (10.91 keV) x-ray source is calculated by the equation

$$\frac{\Phi}{X} = \frac{5.43 \times 10^5}{(\mu[E]/\rho)_{\text{en}} E} \frac{\text{photons}}{\text{mm}^2\ \text{mR}}$$

where Φ is the photon fluence (photons/mm^2) and X is the exposure (mR), where 1 mR = 8.9×10^{-6} Gy$_{\text{air}}$. Φ/X value can be obtained on the basis of previous work (21, 41). Here, we plot the Φ/X for energy between 1 and 30 keV (fig. S12) and fitting the curve with power law

$$f(x) = 1704.67 + 69.618X^{2.2025}$$

Therefore, Φ/X for 10.91 keV can be obtained and the value is 15148.73 photons/mm^2/mRΦ.

On the other hand, taking W_{air} = 33.8 eV, the total exposure can be calculated by

$$X = \frac{\text{total charge ionized}}{\text{total mass}} = \frac{\text{photon flux} \times \frac{\text{Energy}}{W}}{\text{total mass}}$$

Assuming the area is 1 cm^2, and the mass attenuation coefficient for air (10 keV x-ray) is estimated to be 4.72 cm^2/g, the x-ray stopping length is about 1000 cm. The total exposure over the 1-cm^2 area is

$$X = \frac{3.01 \times 10^{12} \times \frac{10910}{33.8} \times 1.6 \times 10^{-19}}{1000\ \text{cm} \times 1.2754\ \text{kg/m}^3} = 0.136\ \text{C/kg}$$

Considering 1 R = 2.58×10^{-4} C/kg, and 1 R = 0.00877 Gy$_{\text{air}}$, the total exposure over air at the maximum photon flux used here is 4.419 Gy$_{\text{air}}$ s^{-1}.

Sensitivity calculation

From x-ray dosage calculation, we have calculated the dosage (Gy$_{\text{air}}$ s^{-1}) for our device under various photon fluxes and also converted the device's current density (A cm^{-2}) into charge density (C cm^{-2} s^{-1}). Therefore, the sensitivity for our device is 0.276 C Gy$_{\text{air}}^{-1}$ cm^{-3}.

SUPPLEMENTARY MATERIALS

REFERENCES AND NOTES
1. A. R. Cowen, S. M. Kengyelics, A. G. Davies, Solid-state, flat-panel, digital radiography detectors and their physical imaging characteristics. *Clin. Radiol.* **63**, 487–498 (2008).
2. M. Hoheisel, Review of medical imaging with emphasis on X-ray detectors. *Nucl. Instrum. Methods Phys. Res. A* **563**, 215–224 (2006).
3. M. J. Yaffe, J. A. Rowlands, X-ray detectors for digital radiography. *Phys. Med. Biol.* **42**, 1–39 (1997).
4. B. G. Durie, S. E. Salmon, High speed scintillation autoradiography. *Science* **190**, 1093–1095 (1975).
5. J. Irvine, M. Young, S. German, R. Eaton, in *2015 IEEE Applied Imagery Pattern Recognition Workshop (AIPR)* (2015), pp. 1–9.

6. D. Mery, V. Riffo, I. Zuccar, C. Pieringer, in *2013 IEEE Conference on Computer Vision and Pattern Recognition Workshops* (2013), pp. 368–374.

7. K. Wells, D. A. Bradley, A review of X-ray explosives detection techniques for checked baggage. *Appl. Radiat. Isot.* **70**, 1729–1746 (2012).

8. T. Hatsui, H. Graafsma, X-ray imaging detectors for synchrotron and XFEL sources. *IUCrJ* **2**, 371–383 (2015).

9. A. Bergamaschi, S. Cartier, R. Dinapoli, D. Greiffenberg, I. Johnson, D. Mezza, A. Mozzanica, B. Schmitt, X. Shi, J. Jungmann-Smith, G. Tinti, X-ray detector development at the swiss light source. *Synchrotron Radiat. N.* **27**, 3–8 (2014).

10. N. Yagi, M. Yamamoto, K. Uesugi, K. Inoue, CMOS imaging detectors as X-ray detectors for synchrotron radiation experiments. *AIP Conf. Proc.* **705**, 885–888 (2004).

11. D. S. McGregor, Materials for gamma-ray spectrometers: Inorganic scintillators. *Annu. Rev. Mater. Res.* **48**, 245–277 (2018).

12. F. J. Ramírez-Jiménez, PIN diode detectors. *AIP Conf. Proc.* **1026**, 213–226 (2008).

13. H. Tsai, W. Nie, J.-C. Blancon, C. C. Stoumpos, C. M. M. Soe, J. Yoo, J. Crochet, S. Tretiak, J. Even, A. Sadhanala, G. Azzellino, R. Brenes, P. M. Ajayan, V. Bulović, S. D. Stranks, R. H. Friend, M. G. Kanatzidis, A. D. Mohite, Stable light-emitting diodes using phase-pure ruddlesden–popper layered perovskites. *Adv. Mater.* **30**, 1704217 (2018).

14. H. Tsai, W. Nie, J.-C. Blancon, C. C. Stoumpos, R. Asadpour, B. Harutyunyan, A. J. Neukirch, R. Verduzco, J. J. Crochet, S. Tretiak, L. Pedesseau, J. Even, M. A. Alam, G. Gupta, J. Lou, P. M. Ajayan, M. J. Bedzyk, M. G. Kanatzidis, A. D. Mohite, High-efficiency two-dimensional Ruddlesden–Popper perovskite solar cells. *Nature* **536**, 312–316 (2016).

15. H. Tsai, R. Asadpour, J.-C. Blancon, C. C. Stoumpos, O. Durand, J. W. Strzalka, B. Chen, R. Verduzco, P. M. Ajayan, S. Tretiak, J. Even, M. A. Alam, M. G. Kanatzidis, W. Nie, A. D. Mohite, Light-induced lattice expansion leads to high-efficiency perovskite solar cells. *Science* **360**, 67–70 (2018).

16. W. Nie, H. Tsai, R. Asadpour, J.-C. Blancon, A. J. Neukirch, G. Gupta, J. J. Crochet, M. Chhowalla, S. Tretiak, M. A. Alam, H.-L. Wang, A. D. Mohite, High-efficiency solution-processed perovskite solar cells with millimeter-scale grains. *Science* **347**, 522–525 (2015).

17. H. Tsai, R. Asadpour, J.-C. Blancon, C. C. Stoumpos, J. Even, P. M. Ajayan, M. G. Kanatzidis, M. A. Alam, A. D. Mohite, W. Nie, Design principles for electronic charge transport in solution-processed vertically stacked 2D perovskite quantum wells. *Nat. Commun.* **9**, 2130 (2018).

18. C. A. Klein, Bandgap dependence and related features of radiation ionization energies in semiconductors. *J. Appl. Phys.* **39**, 2029–2038 (1968).

19. W. Wei, Y. Zhang, Q. Xu, H. Wei, Y. Fang, Q. Wang, Y. Deng, T. Li, A. Gruverman, L. Cao, J. Huang, Monolithic integration of hybrid perovskite single crystals with heterogenous substrate for highly sensitive X-ray imaging. *Nat. Photonics* **11**, 315–321 (2017).

20. S. Shrestha, R. Fischer, G. J. Matt, P. Feldner, T. Michel, A. Osvet, I. Levchuk, B. Merle, S. Golkar, H. Chen, S. F. Tedde, O. Schmidt, M. Rührig, M. Göken, W. Heiss, G. Anton, C. J. Brabec, High-performance direct conversion X-ray detectors based on sintered hybrid lead triiodide perovskite wafers. *Nat. Photonics* **11**, 436–440 (2017).

21. W. Pan, H. Wu, J. Luo, Z. Deng, C. Ge, C. Chen, X. Jiang, W.-J. Yin, G. Niu, L. Zhu, L. Yin, Y. Zhou, Q. Xie, X. Ke, M. Sui, J. Tang, Cs₂AgBiBr₆ single-crystal X-ray detectors with a low detection limit. *Nat. Photonics* **11**, 726–732 (2017).

22. Y. C. Kim, K. H. Kim, D.-Y. Son, D.-N. Jeong, J.-Y. Seo, Y. S. Choi, I. T. Han, S. Y. Lee, N.-G. Park, Printable organometallic perovskite enables large-area, low-dose X-ray imaging. *Nature* **550**, 87–91 (2017).

23. H. Wei, Y. Fang, P. Mulligan, W. Chuirazzi, H.-H. Fang, C. Wang, B. R. Ecker, Y. Gao, M. A. Loi, L. Cao, J. Huang, Sensitive X-ray detectors made of methylammonium lead tribromide perovskite single crystals. *Nat. Photonics* **10**, 333–339 (2016).

24. S. Yakunin, M. Sytnyk, D. Kriegner, S. Shrestha, M. Richter, G. J. Matt, H. Azimi, C. J. Brabec, J. Stangl, M. V. Kovalenko, W. Heiss, Detection of X-ray photons by solution-processed lead halide perovskites. *Nat. Photonics* **9**, 444–449 (2015).

25. M. L. Lucia, J. L. Hernandez-Rojas, C. Leon, I. Mártil, Capacitance measurements of p-n junctions: Depletion layer and diffusion capacitance contributions. *Eur. J. Phys.* **14**, 86–89 (1993).

26. L. J. A. Koster, V. D. Mihailetchi, R. Ramaker, P. W. M. Blom, Light intensity dependence of open-circuit voltage of polymer:Fullerene solar cells. *Appl. Phys. Lett.* **86**, 123509 (2005).

27. R. A. Sinton, A. Cuevas, Contactless determination of current–voltage characteristics and minority-carrier lifetimes in semiconductors from quasi-steady-state photoconductance data. *Appl. Phys. Lett.* **69**, 2510–2512 (1996).

28. J.-C. Blancon, H. Tsai, W. Nie, C. C. Stoumpos, L. Pedesseau, C. Katan, M. Kepenekian, C. M. M. Soe, K. Appavoo, M. Y. Sfeir, S. Tretiak, P. M. Ajayan, M. G. Kanatzidis, J. Even, J. J. Crochet, A. D. Mohite, Extremely efficient internal exciton dissociation through edge states in layered 2D perovskites. *Science* **355**, 1288–1292 (2017).

29. R. L. Owen, J. M. Holton, C. Schulze-Briese, E. F. Garman, Determination of X-ray flux using silicon pin diodes. *J. Synchrotron Radiat.* **16**, 143–151 (2009).

30. E. M. Gullikson, R. Korde, L. R. Canfield, R. E. Vest, Stable silicon photodiodes for absolute intensity measurements in the VUV and soft X-ray regions. *J. Electron. Spectros.* **80**, 313–316 (1996).

31. S. Kasap, Low-cost X-ray detectors. *Nat. Photonics* **9**, 420–421 (2015).

32. C. M. M. Soe, C. C. Stoumpos, M. Kepenekian, B. Traoré, H. Tsai, W. Nie, B. Wang, C. Katan, R. Seshadri, A. D. Mohite, J. Even, T. J. Marks, M. G. Kanatzidis, New type of 2D perovskites with alternating cations in the interlayer space, (C(NH₂)₃)(CH₃NH₃)ₙPbₙI₃ₙ₊₁: Structure, properties, and photovoltaic performance. *J. Am. Chem. Soc.* **139**, 16297–16309 (2017).

33. C. C. Stoumpos, D. H. Cao, D. J. Clark, J. Young, J. M. Rondinelli, J. I. Jang, J. T. Hupp, M. G. Kanatzidis, Ruddlesden–popper hybrid lead iodide perovskite 2D homologous semiconductors. *Chem. Mater.* **28**, 2852–2867 (2016).

34. D. H. Cao, C. C. Stoumpos, O. K. Farha, J. T. Hupp, M. G. Kanatzidis, 2D homologous perovskites as light-absorbing materials for solar cell applications. *J. Am. Chem. Soc.* **137**, 7843–7850 (2015).

35. C. M. M. Soe, W. Nie, C. C. Stoumpos, H. Tsai, J.-C. Blancon, F. Liu, J. Even, T. J. Marks, A. D. Mohite, M. G. Kanatzidis, Understanding film formation morphology and orientation in high member 2D Ruddlesden–Popper perovskites for high-efficiency solar cells. *Adv. Energy Mater.* **8**, 1700979 (2018).

36. H. Tsai, W. Nie, P. Cheruku, N. H. Mack, P. Xu, G. Gupta, A. D. Mohite, H.-L. Wang, Optimizing composition and morphology for large-grain perovskite solar cells via chemical control. *Chem. Mater.* **27**, 5570–5576 (2015).

37. W. Nie, H. Tsai, J.-C. Blancon, F. Liu, C. C. Stoumpos, B. Traore, M. Kepenekian, O. Durand, C. Katan, S. Tretiak, J. Crochet, P. M. Ajayan, M. Kanatzidis, J. Even, A. D. Mohite, Critical role of interface and crystallinity on the performance and photostability of perovskite solar cell on nickel oxide. *Adv. Mater.* **30**, 1703879 (2018).

38. Z. Lian, Q. Yan, Q. Lv, Y. Wang, L. Liu, L. Zhang, S. Pan, Q. Li, L. Wang, J.-L. Sun, High-performance planar-type photodetector on (100) facet of MAPbI₃ single crystal. *Sci. Rep.* **5**, 16563 (2015).

39. S. O. Kasap, J. A. Rowlands, Direct-conversion flat-panel X-ray image sensors for digital radiography. *Proc. IEEE* **90**, 591–604 (2002).

40. Z. Jiang, GIXSGUI: A MATLAB toolbox for grazing-incidence X-ray scattering data visualization and reduction, and indexing of buried three-dimensional periodic nanostructured films. *J. Appl. Crystallogr.* **48**, 917–926 (2015).

41. H. E. Johns, J. R. Cunningham, *The Physics of Radiology* (Charles Thomas, ed. 4, 1983).

42. J. Chabbal, C. Chaussat, T. Ducourant, L. Fritsch, J. Michailos, V. Spinnler, G. Vieux, M. Arques, G. Hahm, M. Hoheisel, H. Horbaschek, R. F. Schulz, M. F. Spahn, Amorphous silicon x-ray image sensor, in *Medical Imaging 1996* (SPIE, 1996), vol. 2708.

43. M. Burgelman, P. Nollet, Admittance spectroscopy of thin film solar cells. *Solid State Ionics* **176**, 2171–2175 (2005).

44. S. S. Hegedus, W. N. Shafarman, Thin-film solar cells: Device measurements and analysis. *Prog. Photovolt. Res. Appl.* **12**, 155–176 (2004).

45. T. Walter, R. Herberholz, C. Müller, H. W. Schock, Determination of defect distributions from admittance measurements and application to Cu(In,Ga)Se2 based heterojunctions. *J. Appl. Phys.* **80**, 4411–4420 (1996).

Citation: H. Tsai, F. Liu, S. Shrestha, K. Fernando, S. Tretiak, B. Scott, D. T. Vo, J. Strzalka, W. Nie, A sensitive and robust thin-film x-ray detector using 2D layered perovskite diodes. *Sci. Adv.* **6**, eaay0815 (2020).

ScienceAdvances

A sensitive and robust thin-film x-ray detector using 2D layered perovskite diodes

Hsinhan Tsai, Fangze Liu, Shreetu Shrestha, Kasun Fernando, Sergei Tretiak, Brian Scott, Duc Ta Vo, Joseph Strzalka and Wanyi Nie

ARTICLE TOOLS	http://advances.sciencemag.org/content/6/15/eaay0815
SUPPLEMENTARY MATERIALS	http://advances.sciencemag.org/content/suppl/2020/04/06/6.15.eaay0815.DC1
REFERENCES	This article cites 41 articles, 4 of which you can access for free http://advances.sciencemag.org/content/6/15/eaay0815#BIBL
PERMISSIONS	http://www.sciencemag.org/help/reprints-and-permissions

Use of this article is subject to the Terms of Service